Additive Influence on Bar-Coated $CH_3NH_3PbI_{3-x}Cl_x$ Perovskite Thin Films

Edwin A. Pineda De La O[a,*] and Alan D. F. Dunbar[b]
[a]*Energy Harvesting Research Group, School of Physics & Astronomy, SUPA, University of St Andrews, North Haugh, St Andrews, Fife, KY16 9SS, United Kingdom*
[b]*School of Chemical, Materials and Biological Engineering, The University of Sheffield, Mappin St, Sheffield, S1 3JD, United Kingdom*

Abstract

Understanding and controlling crystallization during scalable deposition of metal halide perovskites remains a central challenge for large-area device fabrication. In this work, we investigate the influence of small quantities of chemical additives - 1,8-diiodooctane (DIO), hydroiodic acid (HI), and deionized (DI) water - on the structural, morphological, and nanoscale properties of bar-coated $CH_3NH_3PbI_{3-x}Cl_x$ thin films deposited under ambient conditions. Optical absorption measurements reveal negligible variation in the optical bandgap (1.56–1.58 eV), indicating that the additives do not significantly alter the electronic structure of the perovskite. However, synchrotron-based grazing-incidence wide-angle and small-angle X-ray scattering (GIWAXS/GISAXS) demonstrate pronounced modifications in crystallization behaviour and nanoscale domain organization. Additive incorporation reduces the radius of gyration from ~1050 Å (pristine) to ~460–556 Å, indicating smaller and more compact scattering domains. Fractal analysis of GISAXS profiles suggests a transition in growth morphology, particularly for HI-treated films, which approach a mass-fractal regime. Thermogravimetric analysis further reveals accelerated solvent evaporation in additive-containing precursor inks, suggesting modified nucleation kinetics during film formation. Despite minimal changes in stoichiometry, the additives significantly influence film morphology, roughness, and crystallite distribution. These findings highlight the critical role of solvent–additive interactions in governing crystallization pathways during scalable bar-coating of perovskite thin films under ambient processing conditions.

Keywords: *Perovskite, Additives, Bar coating, Characterization*

1. Introduction

Organic-inorganic metal halide perovskites have emerged as promising materials for photovoltaic applications, showing high efficiencies in converting sunlight into electricity [1]. Perovskite solar cells achieved a record efficiency of 27.3 % in 2025 [2], a remarkable leap from their initial efficiency of 3.8% reported in 2009 [1]. The excellent properties of perovskite include solution processability, tunable composition, low processing costs, and overall high efficiency. However, the transition from laboratory-scale spin coating to scalable deposition methods remains one of the most significant barriers to commercialization. Additionally, perovskites decompose easily under humid conditions, light or temperature changes; hence, they are required to be processed in a glovebox or a clean room.

Additive engineering has become a powerful strategy to modulate perovskite crystallization. Additives can be used to control multiple properties, such as the crystallite size and density, and even provide control of the polymorph of a given species [3–5]. A range of additives can be incorporated

* Corresponding author.
E-mail address: ed.de.la.o@icloud.com

Manuscript History:
Received 25 March, 2026, Revised 30 April, 2026, Accepted 7 May, 2026, Published 31 October, 2026
Copyright © 2026 UNIMAS Publisher. This is an open access article under the CC BY-NC-SA 4.0 license.
https://doi.org/10.33736/jaspe.12629.2026

e-ISSN: 2289-7771

into the perovskite precursor ink to minimise losses and enhance the performance of perovskite solar cells [5]. Doping $MAPbI_3$ with Cl^- by substitution of I^- ions to form $MAPbI_{3-x}Cl_x$ [6–9] improved the conductivity and the charge diffusion length without affecting the optical properties [7, 10]. Substituting I^- with Cl^- also prolongs the crystallization process due to the lattice distortion when Cl^- is present. Therefore, the mixed halide perovskite requires about 2–3 hours of annealing [11]. C.H. Tsai *et al.* reported a power conversion efficiency (PCE) of 12.86% by adding 1% DIO to $MAPbI_3$[11]. Using DIO as additive in the perovskite ink increases the coverage and smoothness by stimulating homogeneous nucleation and modifying the interfacial DIO perovskite precursor energy making the crystals grow in contact with the surface. DIO coordinates with Pb^{2+} and therefore modifies the crystallization rate and enhances the formation of stable intermediate structures [11]. J.H. Heo *et al.* reported a PCE of 17.2% using 1 v% of HI. They found that the incorporation of HI into perovskite can recover the methylamine (decomposed product of MAI) into MAI, thereby suppressing the decomposition reaction of $MAPbI_3$ perovskite [12]. HI also improves the solubility of PbI_2 facilitating the formation of a dense pure perovskite [13]. On the other hand, a contradictory effect has been reported suggesting that there is no chemical reaction between HI and perovskite precursors, and that HI is removed from the films during annealing. However, adding 1 v% of HI has an impact on the solubility of PbI_2 [14]. Additionally, D.K. Mohamad *et al.* reported the same concentration as additive in spray-casted perovskite solar cells with a PCE of 11.4% [14]. Deionised (DI) water has been reported as an additive in perovskite solution, which improved the crystallization, the surface coverage, and the stability of the perovskite films. Hydrated perovskites were produced during annealing which were resistant to corrosion by water molecules [15]. X. Gong *et al.* studied the effect of various concentrations of DI water in perovskite solar cells reporting a champion PCE of 16.06% adding 2% DI water [15]. They also reported that increasing DI water concentration decreases the PCE and produces large voids amongst the grains. Techniques such as blade coating, slot-die coating, and bar coating introduce complex, non-equilibrium crystallization dynamics governed by solvent evaporation rates, shear forces, and thermal gradients. Controlling these processes is essential to achieving uniform morphology, low defect density, and reproducible optoelectronic performance over large areas [16–18].

In this work, we investigate the influence of small quantities of chemical additives on the final properties of bar–coated $MAPbI_{3-x}Cl_x$ deposited under ambient conditions. We incorporated 1 wt% DIO, 1% by volume HI, and 2% by volume DI water into the perovskite precursor solutions. These specific concentrations were selected based on their successful use in perovskite solar cells via other deposition techniques, e.g., spin coating, spray coating [14], blade blading [18], providing a useful benchmark for comparison. However, in this study, the $MAPbI_{3-x}Cl_x$ films are deposited by bar coating, a large-area deposition method. The resulting $MAPbI_{3-x}Cl_x$ thin films are then characterized using UV-vis spectroscopy, scanning electron microscopy (SEM), energy dispersive spectroscopy (EDS), AFM synchrotron-based grazing incidence wide angle X–ray scattering (GIWAXS), and grazing incidence small angle X–ray scattering (GISAXS). Precursor ink solutions were analysed using thermogravimetric analysis (GTA). By incorporating chemically distinct additives - DIO, HI, and DI water - we isolate how solvent coordination strength and volatility may modify nucleation density and domain growth. Multi-length scale structural analysis reveals that additive-induced acceleration of solvent evaporation reduces characteristic domain size and alters growth regimes without substantially modifying phase composition or optical bandgap. This study provides mechanistic insight into additive-driven crystallization during scalable deposition and may establish design principles for controlling film formation in industrially relevant perovskite manufacturing.

2. Materials and methods

$MAPbI_{3-x}Cl_x$ precursor ink for air processing was purchased from Ossila Ltd. which contained 3:1 MAI:$PbCl_2$ in 99.9% anhydrous DMF. Prior to use, the precursor solutions were continuously stirred and heated to 70 °C on a hotplate. Glass substrates (Menzel-Glasser) were cleaned before use; first,

they were sonicated for 10 minutes in hot water with Hellmanex solution (Z805939 - Sigma Aldrich), then rinsed twice in boiling deionized water. After that, the substrates were again sonicated in IPA, followed by another rinse in deionized boiling water. Finally, they were dried with compressed air and treated in an oxygen plasma cleaner for ten minutes. During the bar spreading, 10 µl of perovskite ink was deposited on half a glass microscope slide (7.5 cm x 1.25 cm).

Perovskite + DIO (250295- Sigma Aldrich) was prepared by adding 1 wt% of DIO with respect to the perovskite weight [1]. 1% per volume of HI (L10410 57 % w/w aq, soln. - Alfa Aesar) was added to the perovskite ink [2]. Perovskite + deionised (DI) water was prepared adding 2% by volume of DI water with respect to the precursor solution.

SEM images and EDS analysis were obtained with a JEOL Ltd. (Tokyo, Japan) JSM6010LA microscope. UV–visible spectroscopy measurements were acquired using an Ocean Optics (Dunedin, Florida) USB2001 spectrometer and DT–MINI–2–GS combined deuterium–halogen light source. AFM images were obtained by a DIMENSION icon – Bruker using a silicon tip on nitride lever tip. TGA was performed using 10 µl of the precursor solutions were analysed using a TGA–4000 Perkin Elmer. XRD patterns were obtained using a D2 Phaser Bruker diffractometer under monochromatic Cu K–alpha radiation (λ = 1.54184 Å) in a range from 2θ = 5° to 60°. GIWAXS and GISAXS data were acquired at the beamline i22 at the Diamond Light Source experiments. GIWAXS experiments used X–ray at an energy of 10 keV with a distance between the sample and the Pilatus 2M detector of 456 mm. For GISAXS, an energy of 14 keV was used with 9.504 m distance between the sample and the detector.

3. Results and discussion

$MAPbI_{3-x}Cl_x$ films (pristine and with additives: DIO, DI water, and HI) were deposited via bar coating with a speed of 40 mm/s with the substrate heated at T_{sub} = 60 °C and thermal annealing for one hour at 90 °C followed by another hour at 100 °C under ambient environment [19]. All samples in Figure 1a exhibit a well-defined absorption onset at approximately 750 nm, characteristic of tetragonal $MAPbI_3$-based perovskite [1, 20, 21]. The optical band gap E_g was calculated by plotting the square of the absorption against photon energy [22], yielding similar E_g values in the range of 1.56–1.58 eV, for HI E_g = 1.56 eV and for the pristine precursor E_g =1.57 eV, indicating minimal influence of the additives on the electronic structure, similar to E_g values reported for $MAPbI_3$ [23–25].

Overall, GIWAXS radial profiles in Figure 1b show that all samples present strong scattering in the peaks related to the planes (002) and (110) located in $q \sim 0.99$ Å^{-1} and $q \sim 1.0$ Å^{-1} corresponding to the tetragonal phase of the perovskite $MAPbI_3$ [26]. The broad feature which has its maximum intensity at $q \sim 1$ Å^{-1} is in fact composed of some narrower peaks, with peaks evident at both $q = 1$ Å^{-1} and $q \sim 1.05$ Å^{-1} [27]. This observation is consistent with the existence of a series of crystallites within the film having different lattice constants, perhaps due to the coexistence of multiple perovskite phases [28, 29]. As well as the high intensity of the main peak around $q \sim 1.0$ Å^{-1}, some samples present certain features in $q \sim 0.9$ Å^{-1} identified as PbI_2 phase [30], being most intense in the sample with DI water. Lower peak around q ~ 0.42 Å^{-1} is identified as PbI_2–solvent complex [30] -, this sample is the only one which presented this peak. The peak around q ~ 0.5 Å^{-1} is related to Pb^{2+} and it is only present in the pristine sample. The rest values $q > 1.2$ Å^{-1} agree with the peaks reported corresponding to the planes (112), (200), (202), (211), (220) and (004) of tetragonal perovskite [31–33]. These variations suggest minor differences in residual secondary phases or intermediate species, while the overall perovskite crystal structure remains preserved [31].

XRD patterns (Figure 1c) exhibit two dominant diffraction peaks at 14.0° and 28.37°, related to the crystallographic planes of (111) and (202) [21], respectively, related to the tetragonal crystal structure of $MAPbI_3$ [24]. The similarity of XRD patterns across all samples confirms that additive incorporation does not alter the primary crystalline phase. This observation aligns with studies showing that additive engineering, such as phenethylammonium iodide (PEAI) doping or mixed-metal incorporation, preserves the tetragonal perovskite structure without introducing new diffraction peaks [34].

Figure 2 shows post–annealed SEM micrographs of bar-coated $MAPbI_{3-x}Cl_x$ films. Pristine $MAPbI_{3-x}Cl_x$ film exhibits incomplete surface coverage and visible pinholes, a very common challenge in scalable blade-coating deposition [18, 35]. Poor surface coverage and homogeneity are evident on the samples with HI and DI water with darker regions associated with pinholes or discontinuities in the film likely due to irregular crystallization [36]. In Figure 3, AFM topography images of $MAPbI_{3-x}Cl_x$ films were obtained in tapping mode over a scan area of 5 × 5 μm². The film exhibits uniform and compact surface morphology with noticeable pinholes, particularly when HI was added. The pristine film exhibits an RMS roughness of 293.0 nm, while the addition of DIO increases the roughness to 369.6 nm, indicating a more uneven surface. In contrast, the ink with DI water shows a significantly reduced RMS of 181.3 nm. The ink treated with HI produced a film with an intermediate roughness of 305.2 nm. Interestingly, while HI has been employed to improve film coverage in perovskite compositions [12-13], its presence in the $MAPbI_{3-x}Cl_x$ system enhances defect formation rather than suppressing it.

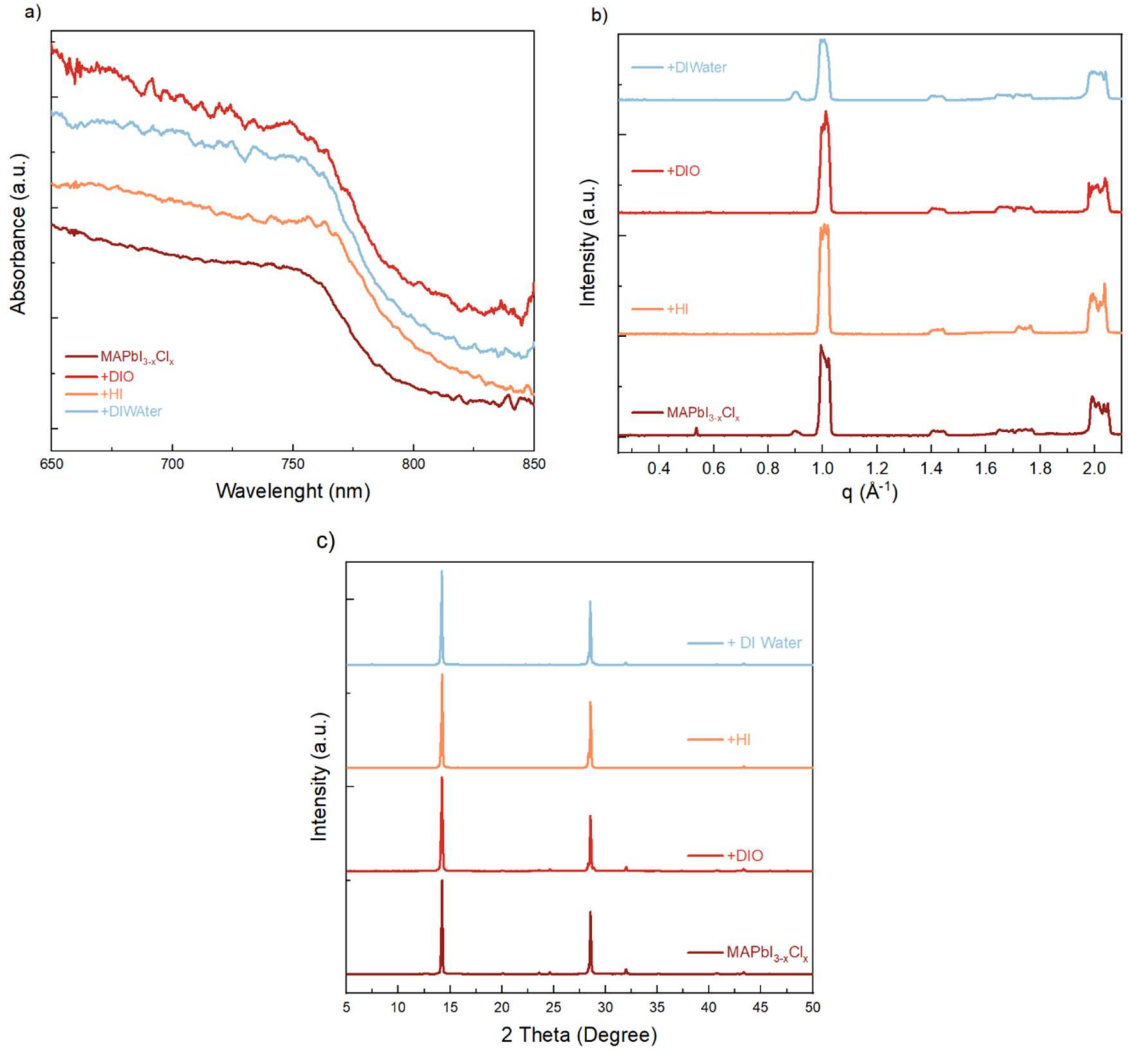


Figure 1. a) UV–vis absorption spectra b) 1D GIWAXS profiles and c) XRD patterns of $MAPbI_{3-x}Cl_x$ films.

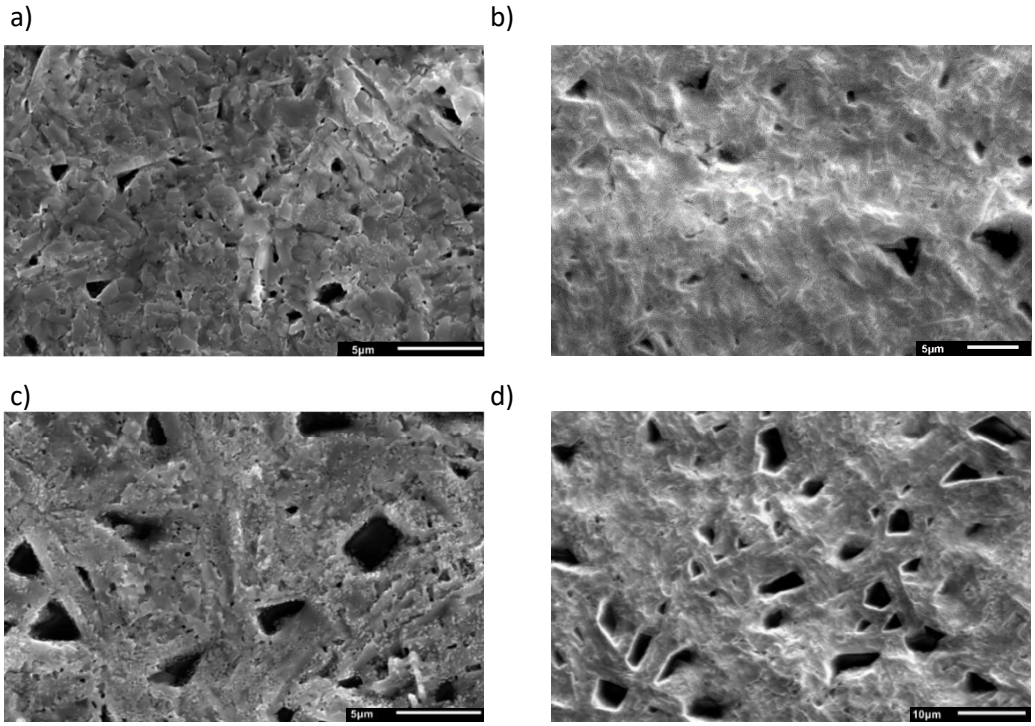


Figure 2. SEM images of a) $MAPbI_{3-x}Cl_x$, b) $MAPbI_{3-x}Cl_x$ + DIO, c) $MAPbI_{3-x}Cl_x$ + HI and d) $MAPbI_{3-x}Cl_x$ + DI water.

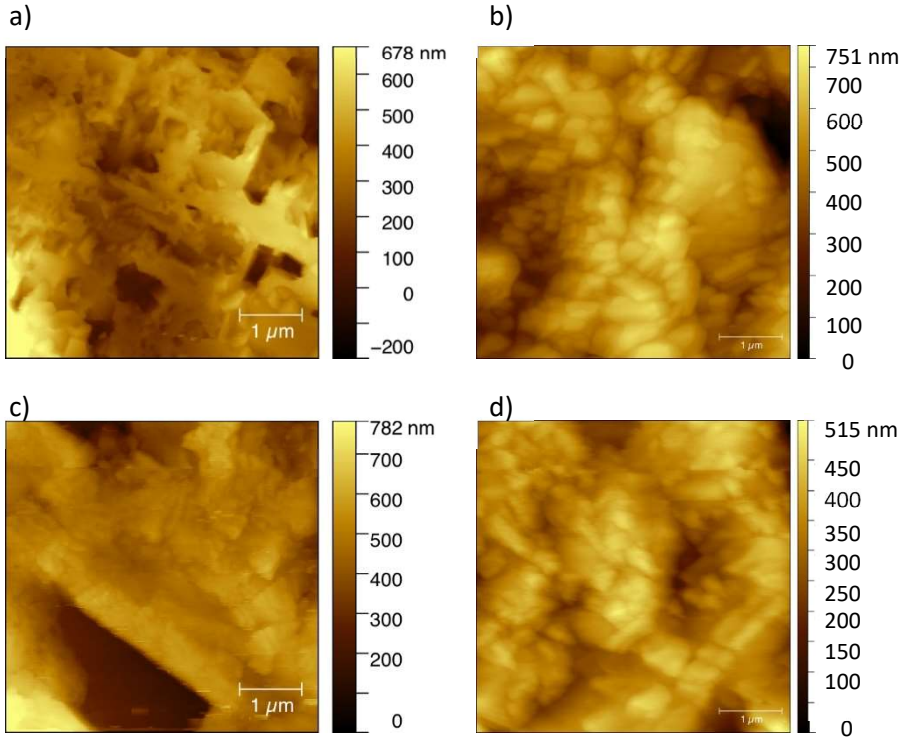


Figure 3. AFM of a) $MAPbI_{3-x}Cl_x$, b) $MAPbI_{3-x}Cl_x$ + DIO, c) $MAPbI_{3-x}Cl_x$ + HI and d) $MAPbI_{3-x}Cl_x$ + DI water.

Figure 4 and Table 1 present the EDS map distribution and the corresponding quantitative elemental composition of $MAPbI_{3-x}Cl_x$ films. All $MAPbI_{3-x}Cl_x$ samples display the expected presence of Pb, I, and Cl, confirming the formation of the perovskite phase. The pristine film shows a Pb:I:Cl ratio of 21.12:75.48:0.30 (%), closely matching the expected stoichiometry of mixed halide perovskite. The presence of chlorine indicates minor retention of Cl^- ions from the precursors after the two hours of annealing in the final crystal structure. This is in agreement with studies showing that Cl in $MAPbI_{3-x}Cl_x$ is not completely expelled but can remain as Cl-rich secondary phase or segregate at grain boundaries [37–39]. The presence of DIO in the perovskite precursor does not significantly alter the composition maintaining the Pb:I:Cl ratio similar to the pristine $MAPbI_{3-x}Cl_x$. In contrast, HI additive induces the most pronounced compositional disturbance. HI noticeably decreases the mass % content of both Pb (19.75%) and I (73.66%), accompanied by a slight increase in Cl (0.35%). This suggests that HI promotes a higher retention of chlorine, possibly by altering the crystallization pathway or by stabilizing Cl-rich secondary phases such as PbICl or $PbCl_2$ [38]. Interestingly, the DI water sample shows a composition nearly identical to the pristine film (Pb 21.12%, I 75.66%, Cl 0.13%), but with the lowest Cl content implying that water may facilitate the removal of chlorine during annealing without altering the Pb–I stoichiometry [40].

Ex situ GISAXS was performed on $MAPbI_{3-x}Cl_x$ samples to probe the influence of additives on structural organization. The in–plane GISAXS profiles were taken for each image by defining a box profile on the right of the image at the Yoneda peak, its decay provides information about film morphology [41]. Figure 5 shows the one-dimensional (1D) GISAXS profiles of the perovskite thin films. The experimental scattering curves were analyzed using both power law and Guinier–Porod models. The Guinier–Porod model is empirical and gives an estimation of the particle size as the radius of gyration R_g of an independent shape representing the average size of scattering domains [42, 43].

Pristine $MAPbI_{3-x}Cl_x$ exhibits a large characteristic R_g = 1051.8 Å, consistent with extended scattering domains and heterogeneous morphology. In contrast, films containing additives show a pronounced reduction in R_g to 660-560 Å. The reduction in R_g domain sizes in the $MAPbI_{3-x}Cl_x$ films with additives may partly be explained by the process of nucleation kinetics during the distribution of the nucleation centres on the substrate. The number of nucleation centres is drastically increased by the presence of the additives in the solution precursor during crystallization [40] and earlier supersaturation onset [27]. This is consistent with earlier *in situ* GISAXS measurements that directly observed an evolution of crystallite sizes and a rise in the number of scattering centres during thermal annealing of $MAPbI_{3-x}Cl_x$ [27].

The power-law fitting provides the exponent α, which describes the surface or interface roughness and the scattering behaviour at large q-values. The resulting parameters are summarized in Table 2. Two regimes are distinguished: if α is in the range $1 \leq \alpha \leq 3$, the film presents mass fractal morphology and if $3 \leq \alpha \leq 4$ is surface fractal. Also, if $\alpha = 4$, the material surface is smooth, while $\alpha = 3$ indicates a rough surface. Additionally, the surface fractal dimension is defined as $D_s = 6 - \alpha$; if this parameter increases, then this indicates that the surface roughness becomes larger. α can also give an estimate of the compactness of the perovskite domain arrangement with a lower value corresponding to a less dense film [42, 43]. The capability of GISAXS to resolve such hierarchical morphologies and fractal structures in perovskite thin films has been well established, allowing a quantitative link between processing conditions and film nanostructure [41, 43].

The pristine $MAPbI_{3-x}Cl_x$ film exhibits $\alpha = 3.41$, indicating a surface fractal structure, with D_s = 2.58 characteristic of a relatively rough surface morphology. The DIO and DI water films show a slightly reduced $\alpha = 3.34$ and $\alpha = 3.18$, respectively. This reduction in domain sizes suggests a denser and more compact nanostructure dominated by smaller, interconnected grains. In contrast, HI has the most pronounced impact, with α = 2.88 corresponding to a mass fractal regime with D_s = 3.11. Physically, this indicates that internal domain structure becomes more heterogeneous and less surface-dominated. Thus, additive incorporation alters the structural evolution of crystallizing domains, the

observed reduction in R_g together with the variations in α indicates a clear modification of mesoscale organization during film formation [27].

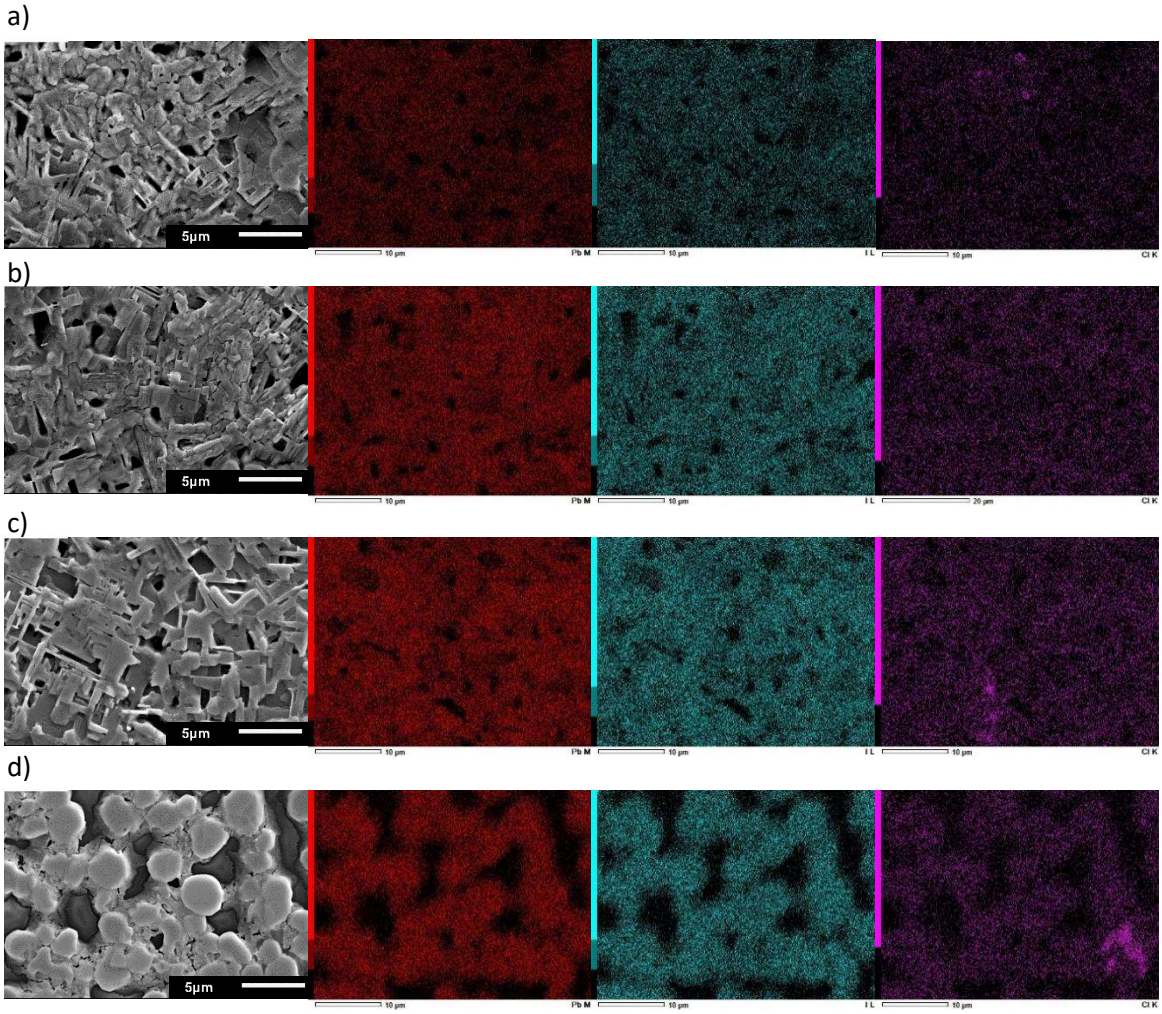


Figure 4. EDS of a) $MAPbI_{3-x}Cl_x$, b) $MAPbI_{3-x}Cl_x$ + DIO, c) $MAPbI_{3-x}Cl_x$ + HI and d) b) $MAPbI_{3-x}Cl_x$ + DI water.

Table 1. % Mass ratio of elements determined by EDS. The other elements counted are C and N with minimal composition.

Material	Pb (%)	I (%)	Cl (%)
$MAPbI_{3-x}Cl_x$	21.12	75.48	0.30
+ DIO	20.78	75.66	0.18
+ HI	19.75	73.66	0.35
+ DI water	21.12	75.66	0.13

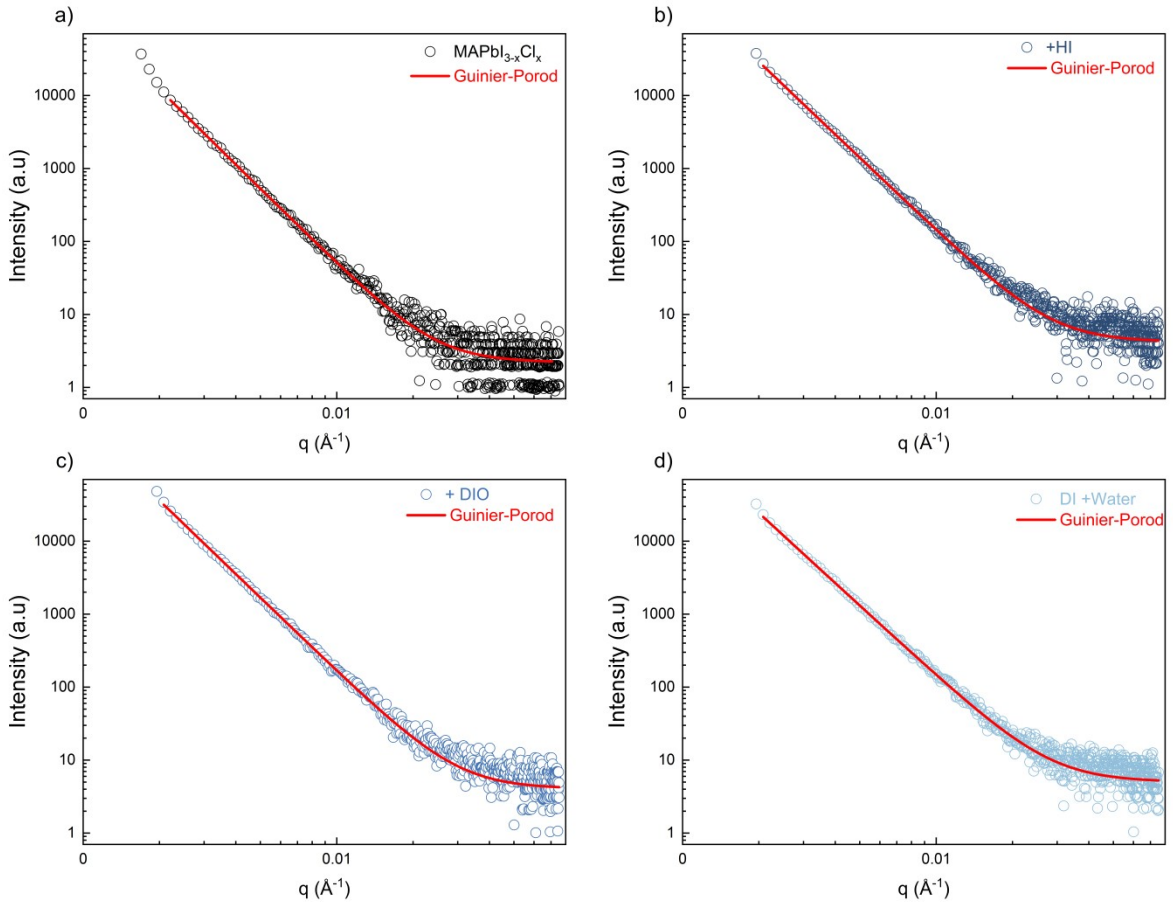


Figure 5. 1D GISAXS profiles for $MAPbI_{3-x}Cl_x$ and additives and their respective fitting curve to the Guinier–Porod model.

Table 2. Parameters obtained from fitting to power law and Guinier–Porod models.

Material	**α**		***Ds* = 6-α**	**R_g (Å)**
$MAPbI_{3-x}Cl_x$	3.41 ± 0.0004	Surface fractal	2.58	1051.8
+ DIO	3.34 ± 0.005		2.65	556.01
+ DI WATER	3.18 ± 0.005		2.81	509.99
+ HI	2.88 ± 0.0043	Mass fractal	3.11	460.58

Thermogravimetric analysis was carried out to monitor the mass loss behaviour of the precursor inks during identical thermal annealing conditions. The TGA profiles in Figure 6 reveal that the additives accelerate the solvent evaporation process. The major mass loss occurs within the first twenty minutes of the experiment, after which the mass remains nearly constant, indicating complete solvent evaporation. All samples, regardless of the additive used, exhibit similar thermal behaviour, with the

initial mass loss corresponding to the evaporation of DMF. The pristine $MAPbI_{3-x}Cl_x$ precursor shows a significant onset of mass loss after approximately four minutes, while the additives clearly accelerate the solvent evaporation process, beginning after two minutes. This difference persists through the early stages of the annealing, where approximately 90% of the total mass loss is reached at ten minutes for the ink with the additive precursors, compared to 12.5 minutes for the pristine one. Complete removal of DMF occurs after roughly 15 minutes in all cases, followed by a stable mass plateau until the end of the measurement. The accelerated solvent evaporation can be attributed to weakened perovskite-DMF interactions and enhanced additive-perovskite precursor interactions, which promote rapid DMF evaporation [40, 44–46].This phenomenon has demonstrated that additives disrupt intermediate solvate phases, thus lowering the energy barrier for solvent removal and accelerating crystallization [40, 44]. Consequently, the additives induce faster attainment of the saturation state and modify the nucleation and crystallization kinetics during film formation [40, 45].

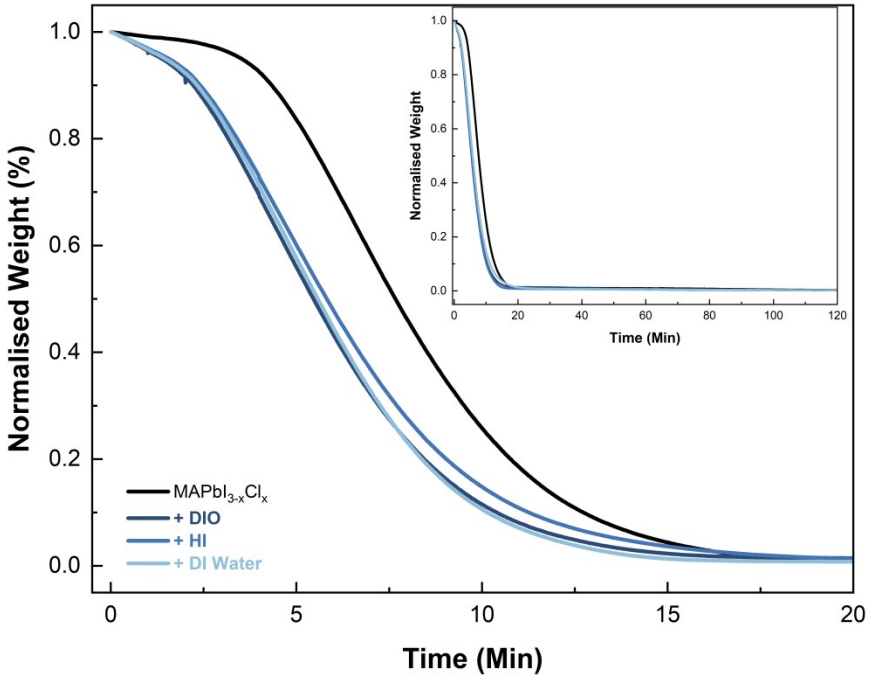


Figure 6. TGA curves for the different precursor solutions. The samples were kept 1 minute at 60 °C, followed by one hour at 90 °C, and finally one hour at 100.

4. Conclusions

This study demonstrates that small concentrations of chemical additives significantly influence the crystallization dynamics and nanoscale morphology of bar-coated $MAPbI_{3-x}Cl_x$ thin films processed under ambient conditions. While optical absorption measurements indicate negligible changes in bandgap energy (1.56–1.58 eV), structural and morphological analyses reveal substantial modifications in growth behaviour.

Synchrotron-based GIWAXS confirms preservation of the tetragonal perovskite phase across all samples, indicating that additive incorporation does not induce phase transitions. However, GISAXS analysis reveals a marked reduction in the radius of gyration from ~1050 Å in pristine films to ~460–556 Å in additive-containing films, indicating the formation of smaller and more compact nanoscale

domains. Fractal analysis suggests that HI-treated films approach a mass-fractal growth regime, whereas pristine films exhibit surface-fractal characteristics. Thermogravimetric measurements demonstrate that additives accelerate solvent evaporation during the initial stages of annealing, shortening the time required to reach supersaturation. This accelerated evaporation likely modifies supersaturation dynamics, increasing nucleation density and altering crystal growth pathways. Despite minimal changes in overall elemental stoichiometry as determined by EDS, the additives influence film roughness, grain distribution, and pinhole formation.

Overall, these results highlight the sensitivity of bar-coated perovskite crystallization to subtle changes in precursor chemistry. The combination of evaporation kinetics modification and nucleation density control provides a mechanistic framework for tailoring film morphology in scalable ambient processing. Understanding these additive-driven pathways is essential for optimizing large-area perovskite thin-film deposition and improving reproducibility in industrially relevant coating methods.

Conflict of Interest

We declare no conflict regarding the publication of the study.

References

[1] Jena, A. K., Kulkarni, A., & Miyasaka, T. (2019). Halide perovskite photovoltaics: background, status, and future prospects. *Chemical reviews*, *119*(5), 3036-3103. https://doi.org/10.1021/acs.chemrev.8b00539

[2] Best Research-Cell Efficiency Chart | Photovoltaic Research | NLR, https://www.nlr.gov/pv/cell-efficiency

[3] Arslan, M., Cai, M., Li, X., Chen, X., Li, Z., & Traore, A. (2025). Additive engineering in crystallization regulation of highly efficient perovskite solar cell. *Materials and Sustainability*, *1*(4), 13. https://doi.org/10.53941/matsus.2025.100013

[4] Tian, Y., Xu, Y., Yin, M. M., Wang, H., Zang, Z., & Mohammed, O. F. (2025). In situ interfacial engineering in perovskite solar cells: The importance of additives. *ACS Energy Letters*, *10*(9), 4102-4130. https://doi.org/10.1021/ACSENERGYLETT.5C02002

[5] Maschwitz, T., Merten, L., Ünlü, F., Majewski, M., Haddadi Barzoki, F., Wu, Z., Öz, S.D., Kreusel, C., Theisen, M., Wang, P., Schiffer, M., Boccarella, G., Marioth, G., Weidner, H., Schultheis, S., Schieferstein, T., Gidaszewski, D., Julliev, Z., Kneschaurek, E., Munteanu, V., Zaluzhnyy, I., Bertram, F., Jaffrès, A., He, J., Ashurov, N., Stolterfoht, M., Wolff, C.M., Unger, E., Olthof, S., Brocks, G., Tao, S., Grüninger, H., Ronsin, O.J.J., Harting, J., Kotthaus, A.F., Kirsch, S.F., Mathur, S., Hinderhofer, A., Schreiber, F., Riedl, T., Brinkmann, K.O. (2025). How crystallization additives govern halide perovskite grain growth. *Nature Communications 2025 16:1*, 16, 9894-. https://doi.org/10.1038/s41467-025-65484-7

[6] Abrusci, A., Stranks, S. D., Docampo, P., Yip, H. L., Jen, A. K. Y., & Snaith, H. J. (2013). High-performance perovskite-polymer hybrid solar cells via electronic coupling with fullerene monolayers. *Nano letters*, *13*(7), 3124-3128. https://doi.org/10.1021/nl401044q

[7] Xing, G., Mathews, N., Sun, S., Lim, S.S., Lam, Y.M., Gratzel, M., Mhaisalkar, S., Sum, T.C. (2013). Long-range balanced electron-and hole-transport lengths in organic-inorganic CH3NH3PbI3. *Science, 342*(6156), 344-347,. https://doi.org/10.1126/science.1243167

[8] Lee, M.M., Teuscher, J., Miyasaka, T., Murakami, T.N., Snaith, H.J., O'Regan, B., Grätzel, M., Green, M.A., Emery, K., Hishikawa, Y., Warta, W., Dunlop, E.D., Han, L., Yella, A., Yu, G., Gao, J., Hummelen, J.C., Wudl, F., Heeger, A.J., Halls, J.J.M., Ip, A.H., Todorov, T.K., Reuter, K.B., Mitzi, D.B., Snaith, H.J., Dennler, G., Scharber, M.C., Brabec, C.J., Hardin, B.E., Snaith, H.J., McGehee, M.D., Bach, U., Burschka, J., Itzhaik, Y., Niitsoo, O., Page, M., Hodes, G., Chang, J.A., Nelson, J., Mitzi, D.B., Field, C.A., Harrison, W.T.A., Guloy, A.M., Chondroudis, K., Mitzi, D.B., Era, M., Tsutsui, T., Saito, S., Kagan, C.R., Mitzi, D.B., Dimitrakopoulos, C.D., Kojima, A., Teshima, K., Shirai, Y., Miyasaka, T., Im, J.H., Lee, C.R., Lee, J.W., Park, S.W., Park, N.G., Chung, I., Lee, B., He, J., Chang, R.P.H., Kanatzidis, M.G., Snaith, H.J., Poglitsch,

A., Weber, D., Leijtens, T., Snaith, H.J., Melas-Kyriazi, J., Abrusci, A., Ding, I.-K., Docampo, P., Barkhouse, D.A.R., Gunawan, O., Gokmen, T., Todorov, T.K., Mitzi, D.B., Kojima, A., Ikegami, M., Teshima, K., Miyasaka, T., Rothenberger, G., Fitzmaurice, D., Graetzel, M., Boschloo, G., Hagfeldt, A., Docampo, P., Bisquert, J., Kavan, L., Grätzel, M., Ishihara, T., Takahashi, J. & Goto, T. (2012). Efficient hybrid solar cells based on meso-superstructured organometal halide perovskites. *Science*, 338, 643–7. https://doi.org/10.1126/science.1228604

[9] Docampo, P., Ball, J. M., Darwich, M., Eperon, G. E., & Snaith, H. J. (2013). Efficient organometal trihalide perovskite planar-heterojunction solar cells on flexible polymer substrates. *Nature communications*, *4*(1), 2761. https://doi.org/10.1038/ncomms3761

[10] Colella, S., Mosconi, E., Fedeli, P., Listorti, A., Gazza, F., Orlandi, F., Ferro, P., Besagni, T., Rizzo, A., Calestani, G., Gigli, G., De Angelis, F. & Mosca, R. (2013). MAPbI3-xClx mixed halide perovskite for hybrid solar cells: The role of chloride as dopant on the transport and structural properties. *Chemistry of Materials*, *25*(22), 4613-4618. https://doi.org/10.1021/cm402919x

[11] Liang, P.W., Liao, C.Y., Chueh, C.C., Zuo, F., Williams, S.T., Xin, X.K., Lin, J. & Jen, A.K.Y. (2014). Additive enhanced crystallization of solution-processed perovskite for highly efficient planar-heterojunction solar cells. *Advanced Materials*, 26(22), 3748–3754. https://doi.org/10.1002/adma.201400231

[12] Heo, J.H., Han, H.J., Kim, D., Ahn, T.K. & Im, S.H. (2015). Hysteresis-less inverted CH3NH3PbI3 planar perovskite hybrid solar cells with 18.1% power conversion efficiency. *Energy & Environmetal Science*, 8(5), 1602–1608. https://doi.org/10.1039/c5ee00120j

[13] Lee, H., Kim, A., Kwon, H.C., Yang, W., Oh, Y., Lee, D. & Moon, J. (2016). Retarding crystallization during facile single coating of NaCl-incorporated precursor solution for efficient large-area uniform perovskite solar cells. *ACS applied materials & interfaces*, *8*(43), 29419-29426. https://doi.org/10.1021/ACSAMI.6B08783/SUPPL_FILE/AM6B08783_SI_003.AVI

[14] Mohamad, D.K., Freestone, B.G., Masters, R., Reinhardt, M., Canning, S., Rodenburg, C. & Lidzey, D.G. (2017). Optimized organometal halide perovskite solar cell fabrication through control of nanoparticle crystal patterning. *J. Mater. Chem. C*, 5(9), 2352–2359. https://doi.org/10.1039/C6TC05189H

[15] Gong, X., Li, M., Shi, X. B., Ma, H., Wang, Z. K., & Liao, L. S. (2015). Controllable perovskite crystallization by water additive for high-performance solar cells. *Advanced Functional Materials*, *25*(42), 6671-6678. https://doi.org/10.1002/adfm.201503559

[16] Tan, W.L., Kirby, N.M., Cheng, Y.B., & McNeill, C.R. (2021). Origin of vertical slab orientation in blade-coated layered hybrid perovskite films revealed with in-situ synchrotron X-ray scattering. *Nano Energy*, 83, 105818. https://doi.org/10.1016/J.NANOEN.2021.105818

[17] Tang, M.C., Fan, Y., Barrit, D., Chang, X., Dang, H.X., Li, R., Wang, K., Smilgies, D.M., Liu, S.F., De Wolf, S., Anthopoulos, T.D., Zhao, K., & Amassian, A. (2020). Ambient blade coating of mixed cation, mixed halide perovskites without dripping: In situ investigation and highly efficient solar cells. *Journal of Materials Chemistry A*, *8*(3), 1095-1104. https://doi.org/10.1039/c9ta12890e

[18] Zhong, J. X., Wu, W. Q., Ding, L., & Kuang, D. B. (2021). Blade-coating perovskite films with diverse compositions for efficient photovoltaics. *Energy & Environmental Materials*, *4*(3), 277-283. https://doi.org/10.1002/EEM2.12118;ISSUE:ISSUE:DOI

[19] Yang, W. S., Noh, J. H., Jeon, N. J., Kim, Y. C., Ryu, S., Seo, J., & Seok, S. I. (2015). High-performance photovoltaic perovskite layers fabricated through intramolecular exchange. *Science*, *348*(6240), 1234-1237. https://doi.org/10.1126/science.aaa9272

[20] Xu, Y., Wang, M., Lei, Y., Ci, Z., & Jin, Z. (2020). Crystallization kinetics in 2D perovskite solar cells. *Advanced Energy Materials*, *10*(43), 2002558. https://doi.org/10.1002/AENM.202002558

[21] Yang, Z., Chueh, C. C., Zuo, F., Kim, J. H., Liang, P. W., & Jen, A. K. Y. (2015). High-performance fully printable perovskite solar cells via blade-coating technique under the ambient condition. *Advanced Energy Materials*, *5*(13), 1500328. https://doi.org/10.1002/aenm.201500328

[22] Jacobsson, T.J., Correa-Baen, J.P., Pazoki, M., Saliba, M., Schenk, K., Gratzel, M., Hagfeldt, A. (2016). Exploration of the compositional space for mixed lead halogen perovskites for high efficiency solar cells. *Energy & Environmental Science*, *9*(5), 1706-1724. https://doi.org/10.1039/c6ee00030d

[23] Huang, Y., Zhang, W., Xiong, Y., Yi, Z., Huang, C., Jiang, Q., Basit, A., Shen, G., Luo, Y., Li, X., & Yang, J. (2025). Recent advancements in ambient-air fabrication of perovskite solar cells. In *Exploration* (Vol. 5, No. 3, p. 20240121). https://doi.org/10.1002/EXP.20240121

[24] Zhang, W., Du, J., Qiu, C., Yang, K., Huang, Q., Wang, Q., Zhang, W., Han, H., Gao, X., & Hu, Y. (2021). Enhanced efficiency of printable mesoscopic perovskite solar cells using ionic liquid additives. *Chemical Communications*, 57(33), 4027–4030. https://doi.org/10.1039/D1CC00169H

[25] Chen, P., Yin, X., Chen, W.H., Song, L., Du, P., Huang, Y., Li, N., Xiong, J. (2021). Perovskite solar cells with PCE over 19% fabricated under air environment by using a dye molecule additive. *Sustain. Energy Fuels*, 5, 2266–2272. https://doi.org/10.1039/D1SE00013F

[26] Song, Z., Sun, K., Meng, Y., Zhu, Z., Wang, Y., Zhang, W., Tian, R., Bai, Y., Lu, X., Yang, M., Liu, C., & Ge, Z. (2025). High efficiency and stable inverted perovskite solar cells enabled by a multifunctional organic salt additive. *Science China Chemistry*, 68(11), 5765–5775. https://doi.org/10.1007/S11426-025-2647-6

[27] Barrows, A. T., Lilliu, S., Pearson, A. J., Babonneau, D., Dunbar, A. D., & Lidzey, D. G. (2016). Monitoring the formation of a CH3NH3PbI3–xClx perovskite during thermal annealing using X-Ray scattering. *Advanced Functional Materials*, *26*(27), 4934-4942. https://doi.org/10.1002/ADFM.201601309

[28] Wu, K., Bera, A., Ma, C., Du, Y., Yang, Y., Li, L., & Wu, T. (2014). Temperature-dependent excitonic photoluminescence of hybrid organometal halide perovskite films. *Physical Chemistry Chemical Physics*, *16*(41), 22476-22481. https://doi.org/10.1039/C4CP03573A

[29] Baikie, T., Fang, Y., Kadro, J. M., Schreyer, M., Wei, F., Mhaisalkar, S. G., ... & White, T. J. (2013). Synthesis and crystal chemistry of the hybrid perovskite (CH3NH3) PbI3 for solid-state sensitised solar cell applications. *Journal of Materials Chemistry A*, *1*(18), 5628-5641.https://doi.org/10.1039/c3ta10518k

[30] Chang, C. Y., Huang, Y. C., Tsao, C. S., & Su, W. F. (2016). Formation mechanism and control of perovskite films from solution to crystalline phase studied by in situ synchrotron scattering. *ACS Applied Materials & Interfaces*, *8*(40), 26712-26721. https://doi.org/10.1021/acsami.6b07468

[31] Qin, M., Chan, P. F., & Lu, X. (2021). A systematic review of metal halide perovskite crystallization and film formation mechanism unveiled by in situ GIWAXS. *Advanced Materials*, *33*(51), 2105290. https://doi.org/10.1002/ADMA.202105290

[32] Steele, J.A., Solano, E., Hardy, D., Dayton, D., Ladd, D., White, K., Chen, P., Hou, J., Huang, H., Saha, R.A., Wang, L., Gao, F., Hofkens, J., Roeffaers, M.B.J., Chernyshov, D., & Toney, M.F. (2023 How to GIWAXS: grazing incidence wide angle X-ray scattering applied to metal halide perovskite thin films. *Advanced Energy Materials*, *13*(27), 2300760. https://doi.org/10.1002/AENM.202300760

[33] Wang, C., Zuo, C., Chen, Q., & Ding, L. (2021). GIWAXS: A powerful tool for perovskite photovoltaics. *Journal of Semiconductors*, *42*(6), 060201.https://doi.org/10.1088/1674-4926/42/6/060201

[34] Magubane, S. S., Arendse, C. J., Ngqoloda, S., Cummings, F., Mtshali, C., & Bolokang, A. S. (2021). Chemical Vapor Deposited Mixed Metal Halide Perovskite Thin Films. *Materials*, *14*(13), 3526. https://doi.org/10.3390/MA14133526/S1

[35] Lee, K. M., Chan, S. H., Hou, M. Y., Chu, W. C., Chen, S. H., Yu, S. M., & Wu, M. C. (2021). Enhanced efficiency and stability of quasi-2D/3D perovskite solar cells by thermal assisted blade coating method. *Chemical Engineering Journal*, *405*, 126992. https://doi.org/https://doi.org/10.1016/j.cej.2020.126992

[36] Deng, Y., Peng, E., Shao, Y., Xiao, Z., Dong, Q., & Huang, J. (2015). Scalable fabrication of efficient organolead trihalide perovskite solar cells with doctor-bladed active layers. *Energy & Environmental Science*, *8*(5), 1544-1550. https://doi.org/10.1039/C4EE03907F

[37] Colella, S., Mosconi, E., Pellegrino, G., Alberti, A., Guerra, V.L.P., Masi, S., Listorti, A., Rizzo, A., Condorelli, G.G., De Angelis, F., & Gigli, G. (2014). Elusive presence of chloride in mixed halide perovskite solar cells. *The Journal of Physical Chemistry Letters*, *5*(20), 3532-3538. https://doi.org/10.1021/JZ501869F

[38] Fan, L., Ding, Y., Luo, J., Shi, B., Yao, X., Wei, C., Zhang, D., Wang, G., Sheng, Y., Chen, Y., Hagfeldt, A., Zhao, Y., & Zhang, X. (2017). Elucidating the role of chlorine in perovskite solar cells. *Journal of Materials Chemistry A*, *5*(16), 7423-7432. https://doi.org/10.1039/C7TA00973A

[39] Vidyasagar, D., Yun, Y.H., Shin, S., Jung, J., Park, W., Lee, J.W., Han, G.S., Ko, C., & Lee, S. (2021). In-situ nano-auger probe of chloride-ions during CH3NH3PbI3−xClx perovskite formation. *Materials*, 14(5), 1102. https://doi.org/10.3390/MA14051102

[40] Pineda De La O, E., Alhazmi, N., Ebbens, S. J., & Dunbar, A. D. (2021). Influence of additives on the in situ crystallization dynamics of methyl ammonium lead halide perovskites. *ACS Applied Energy Materials*, *4*(2), 1398-1409.. https://doi.org/10.1021/ACSAEM.0C02625/SUPPL_FILE/AE0C02625_SI_003.MP4

[41] Schlipf, J., & Müller-Buschbaum, P. (2017). Structure of organometal halide perovskite films as determined with grazing-incidence x-ray scattering methods. *Advanced Energy Materials*, *7*(16), 1700131. https://doi.org/10.1002/AENM.201700131

[42] Liao, H.-C., Tsao, C.-S., Jao, M.-H., Hsu, C.-P., Huang, Y.-C., Tian, K.-Y., Shyue, J.-J., Chen, C.-Y., Su, C.-J., & Su, W.-F. (2015). Hierarchical i–p and i–n porous heterojunction in planar perovskite solar cells. *Journal of Materials Chemistry A*, *3*(19), 10526-10535. https://doi.org/10.1039/c5ta02184g

[43] Huang, Y.C., Tsao, C.S., Cho, Y.J., Chen, K.C., Chiang, K.M., Hsiao, S.Y., Chen, C.W., Su, C.J., Jeng, U.S., & Lin, H.W. (2015). Insight into evolution, processing and performance of multi-length-scale structures in planar heterojunction perovskite solar cells. *Scientific reports*, *5*(1), 13657. https://doi.org/10.1038/srep13657

[44] Xu, C., Zhang, Z., Zhang, S., Si, H., Ma, S., Fan, W., Xiong, Z., Liao, Q., Sattar, A., Kang, Z., & Zhang, Y. (2021). Manipulation of perovskite crystallization kinetics via Lewis base additives. *Advanced Functional Materials*, *31*(13), 2009425. https://doi.org/10.1002/ADFM.202009425

[45] Shargaieva, O., Näsström, H., Smith, J. A., Többens, D., Munir, R., & Unger, E. (2020). Hybrid perovskite crystallization from binary solvent mixtures: interplay of evaporation rate and binding strength of solvents. *Materials Advances*, *1*(9), 3314-3321. https://doi.org/10.1039/d0ma00815j

[46] Alhazmi, N., Pineda, E., Rawle, J., Howse, J. R., & Dunbar, A. D. (2020). Perovskite crystallization dynamics during spin-casting: an in situ wide-angle X-ray scattering study. *ACS applied energy materials*, *3*(7), 6155. https://doi.org/10.1021/acsaem.9b02470